materials

Article

Thermo-Mechanical Simulation of Underwater Friction Stir Welding of Low Carbon Steel

Shabbir Memon [1], Jacek Tomków [2] and Hesamoddin Aghajani Derazkola [3,*]

[1] Department of Mechanical Engineering, Wichita State University, Wichita, KS 67260-133, USA; sxmemon@shockers.wichita.edu
[2] Institute of Machines and Materials Technology, Faculty of Mechanical Engineering and Ship Technology, Gdańsk University of Technology, Gabriela Narutowicza Street 11/12, 80-233 Gdańsk, Poland; jacek.tomkow@pg.edu.pl
[3] Department of Mechanical Engineering, Islamic Azad University of Nour Branch, Nour 21655432, Iran
* Correspondence: h.aghajany@live.com

Abstract: This article investigates the flow of materials and weld formation during underwater friction stir welding (UFSW) of low carbon steel. A thermo-mechanical model is used to understand the relation between frictional heat phenomena during the welding and weld properties. To better understand the effects of the water environment, the simulation and experimental results were compared with the sample prepared by the traditional friction stir welding (FSW) method. Simulation results from surface heat diffusion indicate a smaller preheated area in front of the FSW tool declined the total generated heat in the UFSWed case compared to the FSWed sample. The simulation results revealed that the strain rate of steel in the stir zone (SZ) of the FSWed joint is higher than in the UFSWed case. The microstructure of the welded sample shows that SZ's microstructure at the UFSWed case is more refined than the FSWed case due to the higher cooling rate of the water environment. Due to obtained results, the maximum temperatures of FSWed and UFSWed cases were 1228 °C and 1008 °C. Meanwhile, the simulation results show 1200 °C and 970 °C for conventional and underwater FSW samples, respectively. The maximum material velocity in SZ predicted 0.40 m/s and 0.32 m/s for FSW and underwater FSWed samples. The better condition in the UFSW case caused the ultimate tensile strength of welded sample to increase ~20% compared to the FSW joint.

Keywords: Underwater friction stir welding; process simulation; Material flow; defect analysis

Citation: Memon, S.; Tomków, J.; Derazkola, H.A. Thermo-Mechanical Simulation Underwater Friction Stir Welding of Low Carbon Steel. *Materials* **2021**, *14*, 4953. https://doi.org/10.3390/ma14174953

Academic Editors: Eduardo Garcia, Alberto Murillo-Marrodán and Hamed Aghajani Derazkola

Received: 21 July 2021
Accepted: 27 August 2021
Published: 30 August 2021

1. Introduction

Friction stir welding (FSW) is a relatively new-born solid-state welding technique free from scattering, flash arc, and fume. FSW has several benefits over conventional fusion joining processes [1,2]. The mechanism of base metal (BS) welding is not related to an external heat source, and, for this reason, the properties of BS do not change highly. This feature caused, in some cases, the joint properties to be better than BS [3]. The welding heat is produced by friction at the contact area between the BS and the tool [4,5]. In this situation, the base metal undergoes thermo-mechanical deformation (TMD) by rotational movement of the FSW tool inside of BS. With TMD, fine and equiaxed re-crystallized microstructures form in the joint line and improve the final properties of welded samples [6–11].

Literature has shown that the FSW process is a practical manufacturing process to produce steel structures in an aquatic environment [12]. It is indicated that UFSW controls joint line heat input, and this phenomenon increases the produced weld hardness and mechanical properties [13]. The quality of the UFSWed joint is increased due to the higher rates of cooling at submerging in water [14]. The rotational and traveling velocities of the FSW tool are the main factors in UFSW that determine the quality of joint line materials flow [15]. A comparison of UFSWed and FSWed joint lines showed that submerging in the water prevents the formation of surface oxidation and provides a better surface flow [16]. AA2219 [17–19], AA2519 [20], AA3003 [21], AA5083 [22], AA6061 [23], and AA7055 [24] alloys are aluminum alloys which were experimentally UFSWed. A limited number of studies have reported underwater-FSW dissimilar joining between aluminum-steel [25–27], aluminum-copper [28], and aluminum-magnesium [29,30] with significantly enhanced mechanical properties compared to the regular FSW [23].

Miyamori et al. studied underwater-FSW of medium carbon steel and showed that the underwater-FSW resulted in a slightly rougher appearance than the regular FSW [31]. On the other hand, the UFSW joint exhibits a slightly narrower process window than the FSW one. Due to their results, UFSW leads to higher hardness values in the SZ than FSW case, suggesting that cooling was faster during UFSW. Baillie et al. investigated UFSW of carbon steel and compared output results with FSW of same metal and process parameters [15]. They reported that the UFSW stir zone, thermomechanical affected zone (TMAZ), and heat affected zone (HAZ) appeared to be narrower than the FSW stir zone. They suggested that this was likely caused by the higher quenching rate of the UFSW. Compared to the FSW case, the UFSW stir zone appears to be more homogeneous; meanwhile, no other major defects were detected in either case. Wang et al. improved final properties of friction stir spot welding of advanced ultra-high-strength steel with additional water cooling [32]. According to their report, the mechanical properties of water-cooled welds were significantly improved, and the underwater cooling condition improves surface materials flow. In this regard, flow, thermal properties, and joint mechanism in the UFSWed line are essential aspects that need more consideration. FSW processes have been simulated in various approaches, but simulation of UFSW process has not been undertaken comprehensively. Talebizadehsardari et al. simulated underwater-FSW of 5XXX aluminum alloy by computational fluid dynamics (CFD). They showed that lower preheating area in front of FSW tool is the main factor that caused total heat in UFSW case to be lower than the FSW sample [12]. This result was also reported by Aghajani Derazkola et al. in UFSW of polycarbonate (PC) joint [13]. Sabari et al. implemented the finite element method (FEM) to analyze the underwater-FSW process on the AA2519 aluminum alloy thermally [20]. Hajinezhad and Azizi used the FEM for the thermal study of UFSW of AA6061 aluminum alloy [23]. Aghajani Derazkola et al. analyzed the thermal properties of UFSW of a dissimilar joint between aluminum and steel through CFD [16,26]. Salimi et al. employed the FEM to investigate the residual stress of UFSWed AA6061 aluminum alloy and compared the results with ultrasonic measurement [33]. Owing to limited available research, the behavior of steel joints during underwater friction stir welding has not been reported. Among different type of steels, A441 AISI steel material is widely used in various structures, such as automobile, ship, and train frames. Therefore, this study aims to use the computational fluid dynamic technique to model underwater-FSW process of low carbon steel. The results will be used for the understanding of material flow properties and defect formation in joint lines.

2. Modeling of UFSW Process

2.1. Temperature Field

In this study, velocity and temperature fields were solved under steady state circumstances. Accordingly, the T as transient temperature field was considered as a function of time (t) in the spatial coordinates (x, y, z). The T modelled with the 3D heat transfer nonlinear equation, as presented in [34–36]:

$$k\left(\frac{\partial^2 T}{\partial x^2}+\frac{\partial^2 T}{\partial y^2}+\frac{\partial^2 T}{\partial z^2}\right)+L_{Total}=c\rho\frac{\partial T}{\partial t} \quad (1)$$

In Equation (1), L_{Total} is the heat source that can be calculated by the produced heat at all interfaces of tool and workpiece. In this case, the total heat will be the sum of produced heat by tool shoulder (L_{ts}), tool pin body (L_{pb}), and the tool lower pin beneath (L_{pbs}). The L_{Total} can be presented as [37]:

$$L_{Total} = L_{ts} + L_{pb} + L_{pbs} \tag{2}$$

$$L_{ts} = \frac{2}{3}\pi\omega\left[\delta\tau + \left(1-\delta\right)\mu P\right]\left(R_1^{\,3} - R_2^{\,2}\right) \tag{3}$$

In Equation (3), the ω and P presents the welding tool rotation per minutes and the axial force, respectively. R_1 and R_2 are exterior and interior radii of tool shoulder. The average heat flux at tool shoulder and workpiece is [38]:

$$I_{ts} = \frac{2\omega\left[\delta\tau + \left(1-\delta\right)\mu P\right]\left(R_1^{\,2} + R_2^{\,2} + R_1R_2\right)}{3\left(R_1 + R_2\right)} \tag{4}$$

In Equation (4), the δ represents the mechanical factor, which has a range between 0 and 1. The value of 0 is used for pure sliding condition and 1 is used for pure sticking condition. In this study, the value of δ is selected as 0.32, which shows the best match for the UFSW condition, and 0.41 for the conventional FSW joint. In Equation (4), τ is equal to $\sigma_y/\sqrt{3}$, and σ_y is the yielding strength of steel [39]. Similarly, l_{pb} and l_{pbs} and their corresponding heat fluxes (l_{pb} and l_{pbs}) were calculated by [40]:

$$L_{pb} = \frac{2\delta\pi\omega\tau}{3\tan\alpha}\left(R_2^{\,3} - R_3^{\,3}\right) + \frac{2}{3}\left(1-\delta\right)\frac{\pi\mu P\,\omega}{\sin\alpha}\left(R_2^{\,3} - R_3^{\,3}\right) \tag{5}$$

$$I_{pb} = \frac{(2\delta\omega\tau.\cos\alpha + 2\left(1-\delta\right)\mu P\omega)\left(R_2^{\,3} - R_3^{\,3}\right)}{3\left(R_2^{\,2} - R_3^{\,2}\right)} \tag{6}$$

$$L_{pbs} = \frac{2(\delta\pi\tau\omega + \left(1-\delta\right)\pi\mu P\omega)R_3^{\,3}}{3} \tag{7}$$

$$I_{pbs} = \frac{2\omega R_3}{3}\left(\delta\tau + \left(1-\delta\right)\mu P\right) \tag{8}$$

R_2 is defined as the interior radius of the tool shoulder and is equal to the exterior radius of the pin. R_3 represents the interior radius of the pin and α is FSW pin angle.

2.2. Boundary Conditions

In this study, the temperature of the BS was set at 25 °C (as room temperature) and the temperature of water was also set at 25 °C. Due to the low thermal conductivity of the welding tool compare workpiece, the concentration of heat on the FSW tool is more than base metal. In this regard, the partition of heat between the FSW tool and steel can be calculated by:

$$E = \frac{R_w}{R_w + F_t} = \frac{\left(\sqrt{k\rho C_p}\right)_w}{\left(\sqrt{k\rho C_p}\right)_w + \left(\sqrt{k\rho C_p}\right)_t} \tag{9}$$

In Equation (9), k and Cp show thermal conductivity and specific heat, where w and t represent the workpiece and the tool. R and F represent the fraction of heat entering the workpiece and the generated heat, respectively. The heat transfer at the interface of tool and workpiece can determined by:

$$-k\frac{\partial T}{\partial Z}\bigg|_{Interface} = E \times L_{ts} \tag{10}$$

To simplify the simulation domain and decreasing processing time, the water environment is not considered in the solving domain. Instead of water environment, the heat transfer condition of submerged situation considered in the model. The heat transfer between tool and workpieces in underwater situation is considered [41,42]. At the bottom of base metal, the conductive heat transfer of steel with the fixture plate is determined by [43–46]:

$$k\frac{\partial T}{\partial Z}\bigg|_{Bottom} = h_b\left(T - T_a\right) \tag{11}$$

The h_b (heat transfer coefficient) at the bottom surface is dependent on the local temperature and can be presented as [47]:

$$h_b = h_{b0}\left(T - T_a\right)^{0.25} \tag{12}$$

At the top surface of BS, convective and radiation heat transfer situations are considered as [48,49]:

$$-k\frac{\partial T}{\partial Z}\bigg|_{Top} = \mathrm{B}\epsilon\left(T^4 - T_a^4\right) + h_t\left(T - T_a\right) \tag{13}$$

T_a is the ambient temperature, selected as 298 K. In Equation (13), h_t, B, and ε are convective heat transfer coefficient, Stefan–Boltzmann constant, and emissivity, respectively. According to the assumptions, the heat transfer coefficients at the top surface of the workpiece in FSW and UFSW cases were selected as 300 W/m^2 °C and 500 W/m^2 °C, respectively. In a similar way, the heat transfer coefficients at the bottom surface of BS were considered 12 W/m^2 °C for FSW case and 300 W/m^2 °C for UFSW case.

2.3. Material Flow

The plastic flow in this study was calculated by solving single phase momentum conservation equation that was presented in Equation (12), the i and j = 1, 2, and 3 that denote x, y, and z directions, respectively [50]:

$$\rho\frac{\partial v_i v_j}{\partial x_i} = -\frac{\partial P}{\partial x_j} + \frac{\partial}{\partial x_i}\left(\varphi\frac{\partial v_i}{\partial x_j} + \varphi\frac{\partial v_j}{\partial x_i}\right) - \rho V_1\frac{\partial v_j}{\partial x_1} \tag{14}$$

The ρ and v are material density and velocity, and V_1 represents the welding tool velocity along the joint line. φ indicates non-Newtonian viscosity which is obtained from σ_e (flow stress) and $\dot{\varepsilon}$ (effective strain rate) [51]:

$$\varphi = \frac{\sigma_e}{3\dot{\varepsilon}} \tag{15}$$

$$\sigma_e = \frac{1}{\gamma} arc\sinh\left(\frac{Z}{A}\right)^{\frac{1}{n}} \tag{16}$$

The γ, A, and n are materials constant, Z is the Zener–Hollomon parameter, which is related to the effective strain rate and can be presented by [52]:

$$Z = \dot{\varepsilon}exp^{\left(\frac{Q}{RT}\right)} \tag{17}$$

In Equation (17), ($\dot{\varepsilon}$) is the effective strain rate, *Q* denotes activation energy, and *R* is universal gas constant [51]:

$$\dot{\varepsilon} = \left(\frac{2}{3}\varepsilon_{ij}\varepsilon_{ij}\right)^{\frac{1}{2}} \tag{18}$$

where ε_{ij} is the strain rate tensor [53]:

$$\varepsilon_{ij} = \frac{1}{2}\left(v_{i,j} + v_{j,i}\right) \tag{19}$$

2.4. Material Properties

Due to the changes in physical properties in the metals, temperature relation properties were set for the workpiece and tool during the welding process. Specific heat (C_P) and thermal conductivity (*K*) equations for A441 AISI steel alloy are defined as [54]:

$$C_p = 412.3 - 8.2T + 3.0\times10^{-4}T^2 + 1.9\times10^{-7}T^3 \tag{20}$$

$$K = 3.6 + 0.09T - 1.72\times10^{-4}T^2 + 7.9\times10^{-8}T^3 \tag{21}$$

Similarly, for the FSW tool that was selected as tungsten made material [54–57]:

$$C_p = 158 + 10.6T - 1.63\times10^{-5}T^2 \tag{22}$$

$$K = 0.367 - 2.29\times10^{-4}T + 1.25\times10^{-7}T^2 \tag{23}$$

For increasing precision of the model results, the density and Young's modulus changes in various temperatures are used during simulation [58]. The FSW tool during the welding process passed three main phases. The first step is known as the plunging stage, which refers to the BS penetration by the welding tool. The second step is stirring the base metals during the transverse movement of the FSW tool, and the third step is the FSW tool exit from the joint line when the welding procedure is finished. For simplicity of simulation procedure, the tool plunging and tool exit steps have not been considered. According to the experimental tests, all parameters (tool geometry, tool rotational and forward velocities, tool tilt angle, and plunge depth) are selected. The tetrahedral/hybrid elements with T-grid combination shapes were used for the mesh generation of tool and work pieces. The region closest to the pin tool and the FSW tool required a much finer mesh to evaluate the heat transfer model and viscous flow. A sizing function on the tool and workpiece was used to generate the different volume sizes. The ultimate number of meshes for the simulation in this study was 960,126 volumes. The equations were solved by ANSYS Fluent commercial software. The simulation was tested by try and errors technique (several times) to validate the obtained results by experiment. The total errors during the simulation procedure were lower than 4% [59,60]. Furthermore, the simulation results converged after 54 iterations for each case. The schematic graph of the FSW area and the isometric view of the meshed domain are presented in Figure 1.

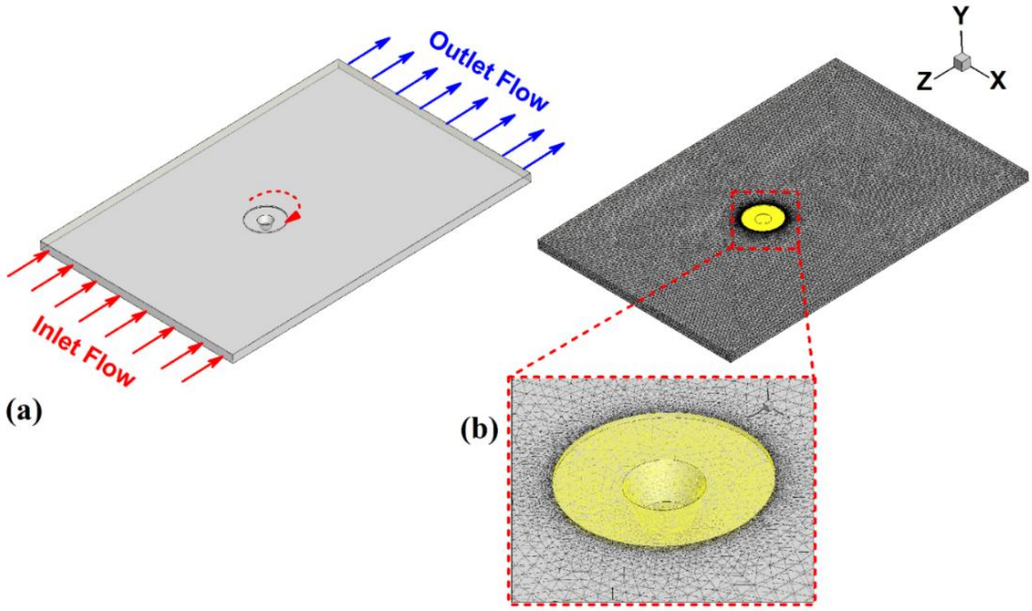

Figure 1. (**a**) Schematic view of the FSW domain. (**b**) Meshed domain.

3. Experimental Procedure

For the welding procedure, 60 pieces of A441 AISI steel were considered. This number was applied for both regular and underwater FSW cases. The welding piece's dimension was 4 × 120 × 100 mm^3. The A441 AISI steel chemical compositions and mechanical properties are presented in Tables 1 and 2, respectively. The results of Tables 1 and 2 were tested by the authors and the results are reported in the paper. A flexible welding setup was made to fix the BS sheets during the FSW process. The fixture was surrounded by Plexiglass plates for submerging of welding system into water. An input and output valve was placed in a Plexiglass box for inlet flow and outlet flow of water. During the experimental procedure, the temperature of the water was at an ambient temperature (28 °C). The used FSW tool had a frustum pin and was made by tungsten. The selected UFSW process parameters in this study are presented in Table 3. For monitoring of thermal history during welding process, K-type thermocouples (Omega, OH, USA) were placed at various positions near the joint line. A virtual measuring machine (VMM) was employed to study the flow of material at the surface of the joint line and optical microscopy was used for the metallographic analysis of the welded samples. For microstructure investigation, Nital Etch solution was used. To study crack formation at the joint line, a radiographic non-detractive test (RT) was implemented on the joint line. The graphical view of the FSW setup, the welding tool geometry, and the position of the thermocouples are described in Figure 2.

Table 1. Chemical composition of the A441 AISI steel.

Element	Si	Cu	Mn	C	P	S	Fe
Value	0.4	0.2	1.0	0.22	0.04	0.05	Balance

Table 2. Mechanical properties of the A441 AISI steel.

Parameter	Density	MP (Melting Point)	UTS (Ultimate Tensile Strength)	Elongation	Hardness
Value	7800 Kg/m^3	1450 °C	580 MPa	15%	182 HV

Table 3. Welding process parameter.

Parameter	Tool Rotational Velocity	Tool Travelling Velocity	Tool Tilt Angle	Tool Plunge Depth
Value	900 rpm	60 mm/min	2.5°	0.2 mm

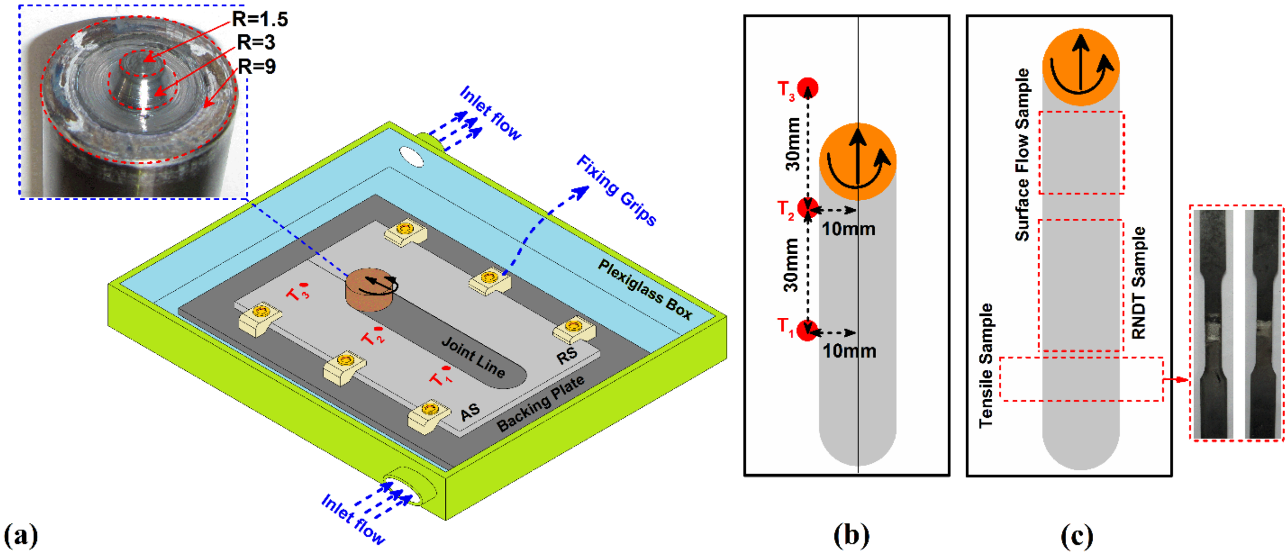

Figure 2. (**a**) Schematic view of welding setup, (**b**) thermocouples position, and (**c**) mechanical test sampling.

4. Results and Discussions

4.1. Thermal Study

The total generated heat during UFSW/FSW is dependent on the many mechanical parameters [61–63]. The used term of ¨heat production ratio¨ here refers to the ratio of the total heat generated by each part of the tool in the both the regular and underwater-FSW cases [32,64]. The heat production rate in all parts of the tool depends on the contact area of tool parts with the base metal. The simulation results indicated that the maximum heat amount was generated in the touch surface of tool shoulder and base metal. Simulation results indicated the amount of produced heat by tool shoulder in FSW is equal to 75% (~900 °C) of total amount of generated heat and, in the UFSW case, the amount of produced heat by tool shoulder is 81% (~786 °C) of total generated heat (Figure 3a). Due to simulation results the generated heat with the pin of FSW tool is less than the amount of heat generated with the FSW tool shoulder. The heat generated by the tool pin area in FSW case is approximately 300 °C and it is near to 25% of the total generated heat.

The generated heat by tool pin in the UFSW case is near to 19% (~115 °C) of the total generated heat in this case. The results of the generation heat showed that the lower contact area by workpiece caused lower heat generation by tool pin in both cases. Figure 3b,c show the thermocouples recorded data in FSWed and UFSWed samples at advancing side (AS). The presented data give information from both AS and retreating side (RS) of joint line. Due to obtained results, the maximum recorded temperature at FSWed and UFSWed cases were 1228 °C and 1008 °C, respectively. These numbers were obtained from thermocouple number T1, which exposed the heat concentration at AS. The comparisons between maximum temperature obtained by simulation and experimental measurement are presented in Figure 3d. Evaluation of obtained results (experimental and simulation) indicated more frictional heat concentration in AS compared with RS due to rotational direction of welding tool. By increasing the distance from T1 to T2, the recorded temperature decreased. It could be traced to heat transfer from joint line with base metal and with environment. The decrease of recorded heat in both AS and RS could be detected. On the other hand, the difference between T1 and T2 temperature in UFSWed sample was more than the FSWed sample. It seems this is the result of higher heat transfer of water environment at UFSWed sample compared to air environment at FSWed sample. This phenomenon shows cooling rates of joint line in UFSWed sample was higher than the FSWed joint. On the other hand, the recorded temperature by T3 indicated that diffused heat from the joint line in leading edge (LE) of tool at FSW case was more than the UFSW case. The internal heat flux of FSWed and UFSWed cases are presented in Figure 3e. The recorded and simulated results from thermocouples T2, T4, and T5 are presented in Figure 3e. Due to obtained results, the heat loss in the UFSW case was more than the FSW sample, which indicates higher cooling rates of the water environment compared to the air environment [65,66].

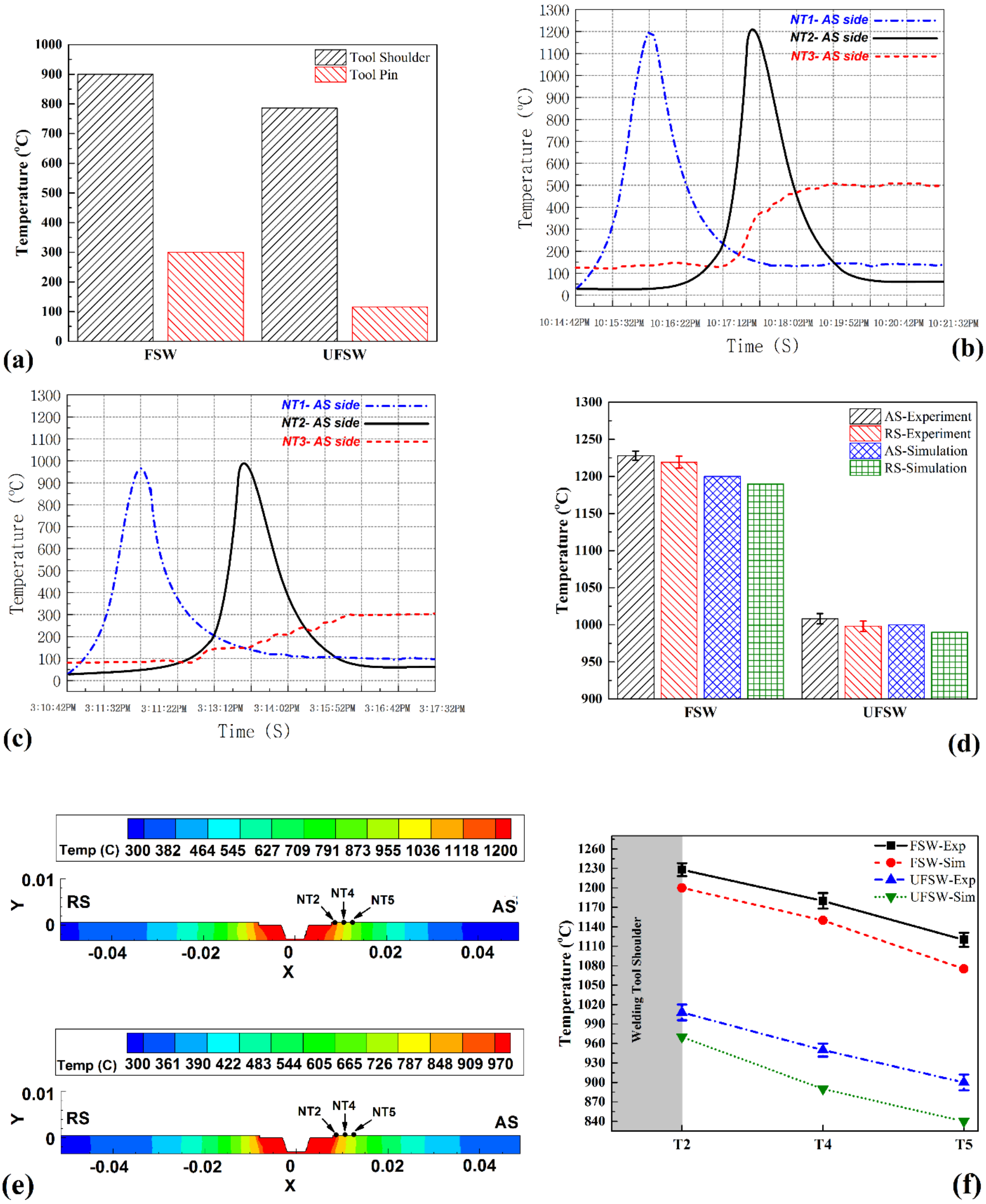

Figure 3. (**a**) Comparison of heat generation rate by different area of tool. Thermal history of (**b**) FSW and (**c**) UFSW samples. (**d**) Comparison of maximum recorded and simulated heat at RS and AS. (**e**) Simulation results of internal heat flow. (**f**) Comparison between recorded and simulated results of cooling rate.

The results of surface heat flux from simulation at underwater-FSWed and regular FSWed samples are shown in Figure 4. Additionally, the experimental results support this phenomenon. The results from simulation also indicated higher generated heat concentration in the top surface of FSWed joint in comparison with the UFSWed case. This phenomenon related to the high heat transfer of the water environment compared to the atmosphere. During the forward movement of welding tool, the raw metal from the LE of the welding tool extruded inside of the SZ. Closer examination of the simulation results indicated that the preheated zone (PHA) at LE in underwater-FSW case was thinner than the FSW case. Thicker PHA can increase probability of the flash formation in the vicinity of the weld line. Control of frictional heat production and more heat transfer in underwater-FSWed joint avoided the excess flow of plasticized steel around the weld line. As a result, the lower surface flash in underwater-FSWed case reduced the probability of joint thinning. Furthermore, lower PHA led to the extrusion of steel metal with higher shear strength (viscosity) from LE into SZ. These results demonstrated why the generated frictional heat in UFSWed joint was lower than the FSWed case. In the UFSW case, the welding tool was required to exert more shear stress in SZ, to convert steel into a fully plasticized shape.

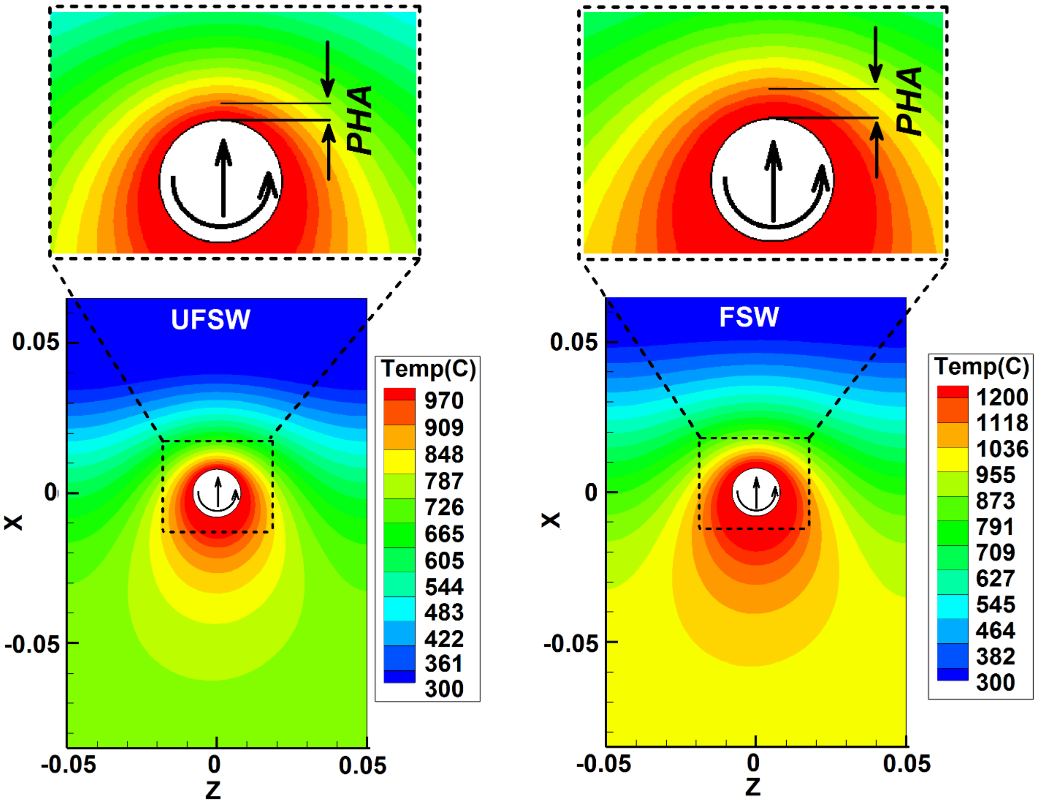

Figure 4. Simulation results of internal heat flow at FSW and UFSW cases.

4.2. Velocity of Material

Figure 5a depicts the results of the plasticized steel velocity simulation in stir zone. The results from simulation show the maximum materials velocity predicted at the tool shoulder exterior area. It seems that the applied higher momentum at the exterior edge (outer area) of shoulder caused the material velocity in the outer area of the shoulder to become more than other areas. These results were predicted in both UFSWed and FSWed samples.

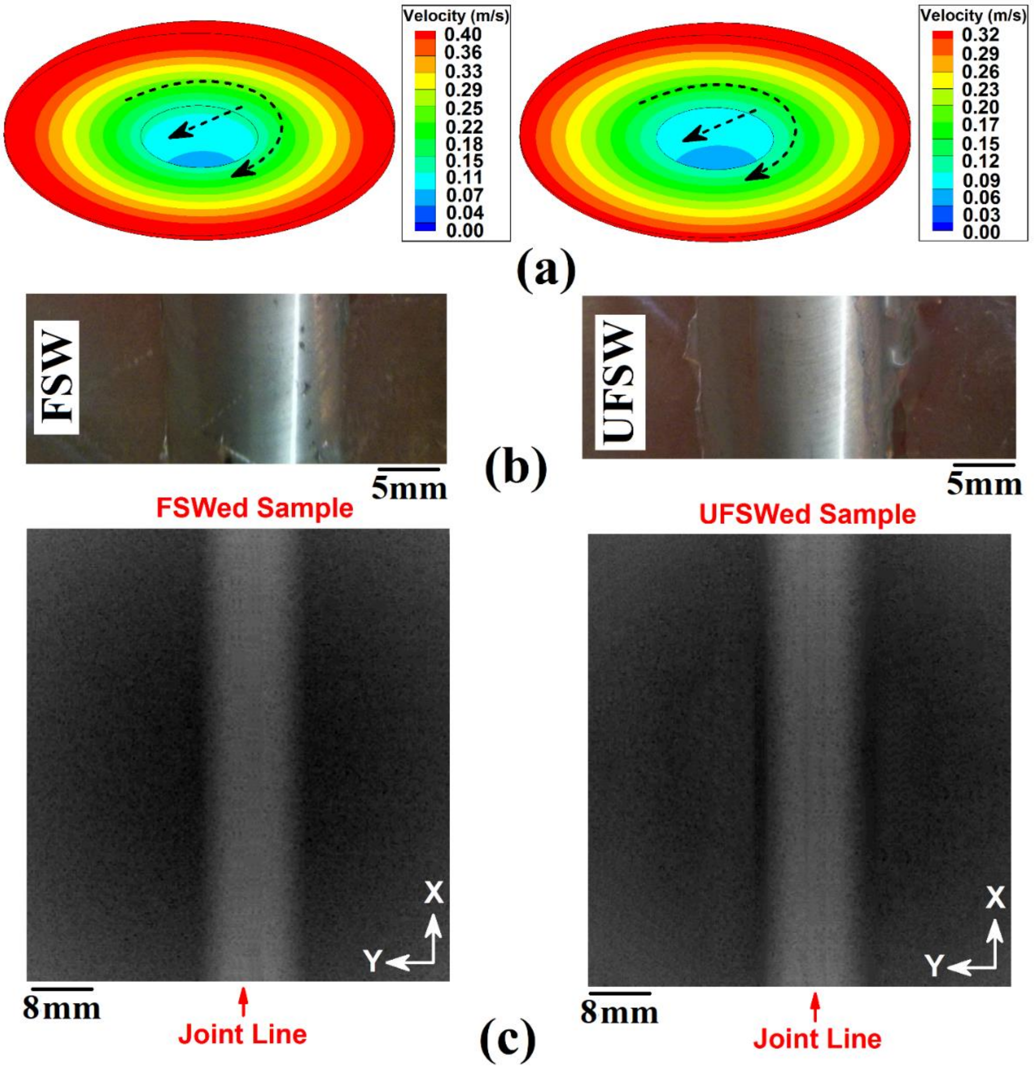

Figure 5. (**a**) Material velocity result from simulation in the SZ of underwater-FSWed and FSWed samples. (**b**) Surface flow of joint lines in both cases. (**c**) Radiography NDT results of joint lines.

As the distance from the edge of the tool shoulder to the center of the SZ decreases, the material velocity decreases. Declining material velocity is due to the decreasing applied momentum near the SZ axis. The simulation results indicated that the velocity of materials in the regular FSW case was more than the underwater-FSW sample. Furthermore, the maximum velocity of steel was predicted as 0.40 m/s and 0.32 m/s in the SZ at regular and underwater FSW conditions, respectively. The higher heat generation and lower cooling rate in the FSW case led to the higher material velocity in SZ. The image of the surface material flow on the joint lines is presented in Figure 5b. Due to obtained results, the ring angle of steel flow (flow curves at surface of joint line) in the UFSWed case is less than FSWed joint. It seems this is the result of lower velocity of steel during the stirring action and the forward movement of the FSW tool in the underwater case [67,68]. The advanced velocity of steel at the regular FSW joint caused the fast transmission of the plasticized materials from the AS to the RS during the forward moving of the FSW tool. Consequently, large angle flow rings are formed in the FSW case. This phenomenon reveals the formation of the weld line at the trailing edge (TE) of the welding tool is easier in the regular FSW case compared to the underwater-FSW joint. The lower heat production and velocity of BS in stir zone of the underwater case delayed the material revolution, leading to flow rings with smaller angles. The radiographic images of joint lines are depicted in Figure 5c. Due to obtained results, any defects in macro-scale were not detected.

4.3. Streamlines and Strain Rate

In this section, the material flow is studied by plotting the cross and longitudinal sections of streamlines in joint area (Figure 6a,b). The streamline pattern (as flow of plastic material) indicated the plasticized steel had started to rotate from AS and was pushed into RS by the tool in both cases. Longitudinal section of streamlines path revealed the pasty steel rotated by tool shoulder from the LE with velocity same as the welding speed, and then pushed (reflow) contrary to TE. The flow of streamlines is denser and closely packed circular lines near the LE at UFSW case compared to the FSW sample. The streamlines occupy a larger area in the FSW case due to the higher momentum transfer and material velocity.

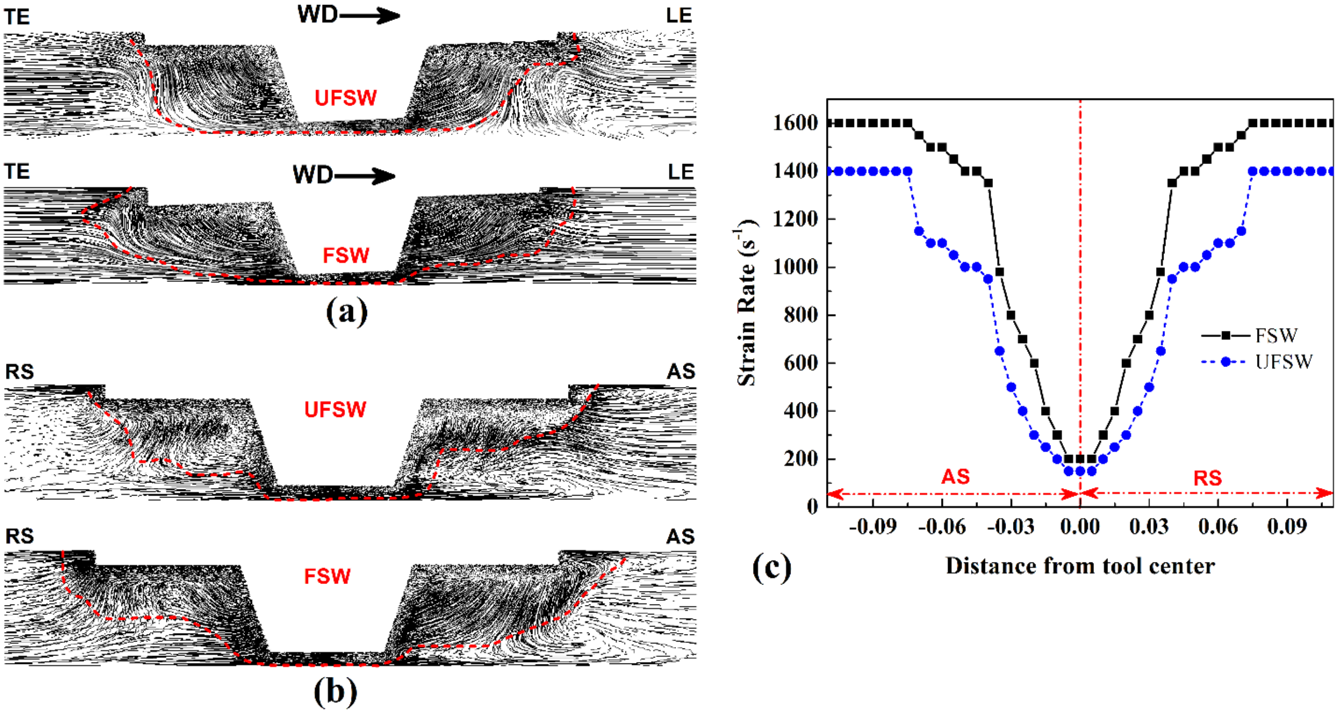

Figure 6. Streamline flow in (**a**) longitudinal section and (**b**) cross section view. (**c**) Variations of strain rate in SZ of the FSW and UFSW samples.

This phenomenon in the UFSW case leads to the formation of smaller SZ compared to the FSW case. It seems this material's behavior is resultant from the higher viscosity of steel in UFSW case. Obviously, during FSW of higher strength metals, lower plastic flow can be attained [69–72]. The simulation result of the strain rate in both FSWed and UFSWed cases are shown in Figure 6c. The value of strain-rate is maximum at the top of the joint and decreased in the lower area of the SZ at both cases. Lower frictional heat generation and velocity of material in the UFSW leads to the maximum value of strain rate in the UFSW case being lower than the FSW case. The simulation results show that maximum strain rate is predicted at the surface of shoulder on the advancing side in all samples.

4.4. Microstructure Changes

The generation of heat in UFSW/FSW process is considered as a function of viscosity and the effective strain rate as discussed before in the modelling section. The results of simulation from viscosity changes in the welding area of FSWed and UFSWed cases are depicted in Figure 7a,b. For a better understanding of the viscosity changes along joint line (from AS to RS), a virtual line was considered at the top area of SZ. According to the obtained results, the viscosity in AS was lower than RS in both cases. As expected, higher heat consideration and strain rate at AS decreased viscosity in this area compared to RS. The distribution of the $\dot{\varepsilon}$ on AS and RS of the tool seems to be symmetrical and peak values of strain rate was around 1600 s^{-1} in the FSW case and 1400 s^{-1} in the UFSW sample, at near the tool shoulder exterior edge. Comparing viscosity shows that the material's viscosity in the UFSW case was more than the FSW. These viscosity changes are directly related to the flow stress and strain rate, so considering the strain and temperature values can be explained by the viscosity difference at FSW and UFSW samples.

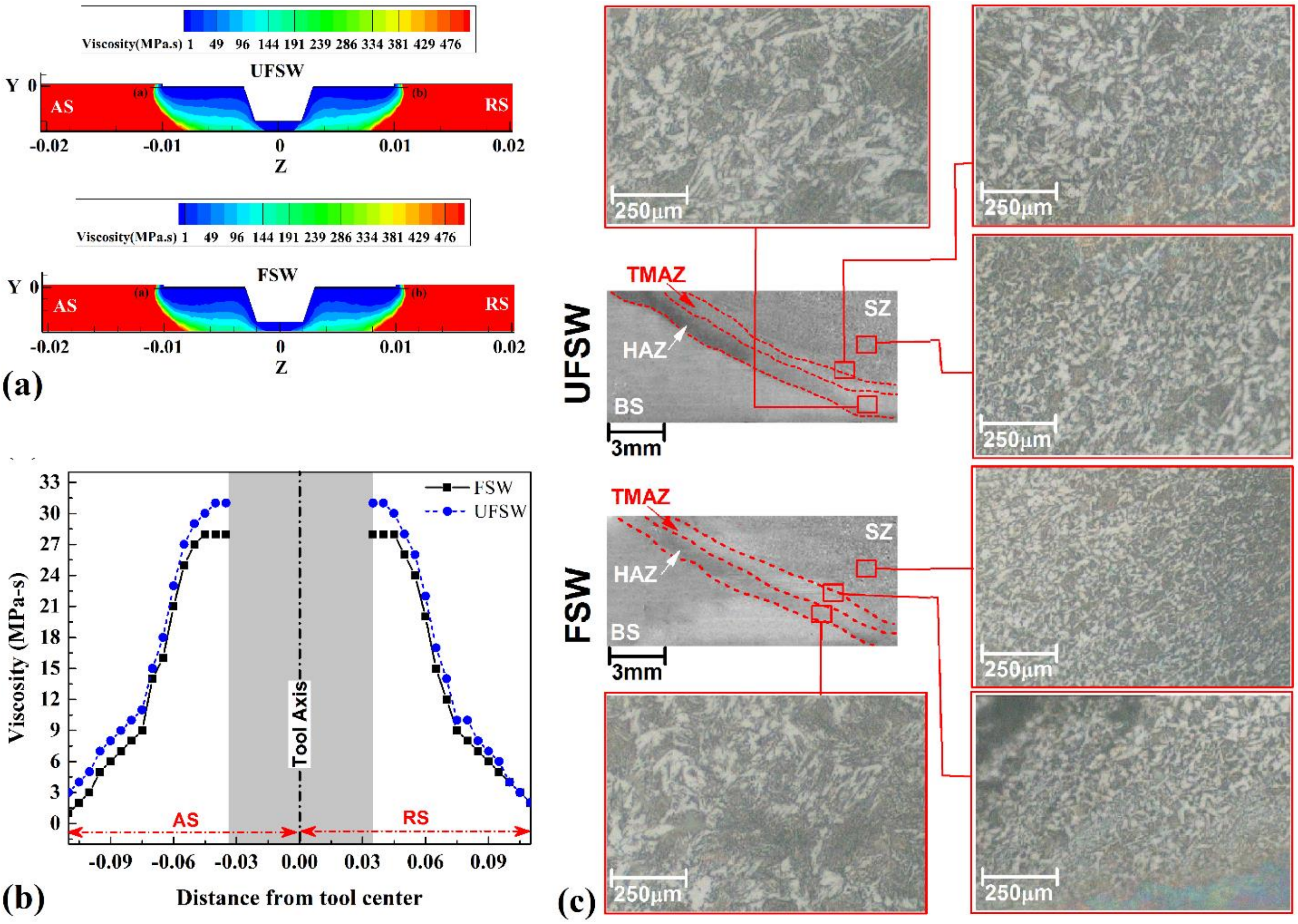

Figure 7. (**a**) Results of viscosity variations from simulation in welded samples. (**b**) Numerical analysis of viscosity changes along line (**a**,**b**) and (**c**) microstructure of welded joints.

A cross-sectional view of the FSWed region is given in Figure 7c. No macro or micro defects were detected in the weld cross section. It has been previously seen in RT results that there is not any defect in joint line. The microstructure of base metal consisted of equiaxed and elongated ferrite grains (~80%) and pearlite phase (~20%) with 11 µm average grain size. In friction stir joints, the heat affected area (HAZ) is a region that does not tolerate plastic deformation cycle but is affected by diffused heat from SZ [73,74]. With a comparison of FSW joint and UFSW, it is revealed that the HAZ area in UFSW case is formed more narrowly than the FSW case. In the UFSW case, plus high cooling rate, the produced frictional heat in SZ was not high enough for grain coarsening in HAZ area, which is common in the FSW joint. The microstructure of HAZ in the FSW case is not same as the UFSW sample. In HAZ region of FSWed sample, pearlites were dissolved and globalization of cementite phases was detected. The SZ of FSWed sample consisted of ferrite, cementite clusters (FC), Widmanstatten, refined ferrite, and pearlite grains. In the UFSW case, small length ferrites and pearlites phases were formed by the low growth of ferrite structures at high cooling rates. A big difference between SZ of FSWed and UFSWed cases is the presence of martensitic phase in the FSWed case, which indicated that the cooling rate of the joint line was probably high enough for martensitic transformation to take place. The study on microstructure evaluation of FSW and UFSW cases indicated that the strain rate has a direct impact on microstructure. In the UFSW case, the total frictional heat was lower than the FSW case. On the other hand, the cooling rate of the UFSW sample was more than the FSW. The point is that the tool velocities during both cases were the same and mechanical action of the tool in all samples was the same. In these regards, it can be concluded that with keeping constant the mechanical cycle of SZ, the generated heat can be influenced in submerged case. Consequently, the thermal cycle and cooling rate of the joint line determines the final microstructure properties of SZ.

4.5. Mechanical Properties

The hardness profiles of welded joints depicted in Figure 8a. The hardness was measured 1 mm below or at the joint crown. The hardness of the joint area increased significantly in the stir zone at both cases. The average hardness of the BS was recorded near 182 HV. The average hardness increased near 240 HV in stir zone of FSWed sample. The hardness increase in the weld region seems to be the result of grain refinement due to extensive plastic deformation followed by dynamic recrystallization. This increase is the result of microstructural changes in this area. Smaller grain size caused the hardness of stir zone to increase to 255 HV. Significant hardness decrease was not detected at the HAZ in either sample, which is usually encountered in FSW of aluminum alloys. The hardness values of HAZ in the UFSWed case was almost similar to the base metal. Figure 8b shows the stress–strain curves obtained from the raw steel specimen, FSWed, and UFSWed samples. Due to obtained results the UTS (ultimate tensile strength) of the FSWed case was near to 71% (~412 MPa) of the base metal. The UTS of UFSWed sample was approximately 84.5% (~490 MPa), and, compared to the FSWed sample, the strength of the UFSWed sample improved 13.5%. The SEM image from fracture surface of welded samples is depicted in Figure 8c. The microscopic investigation from fracture surface showed deep dimples in the fracture surface of both samples, which indicated ductile fracture mode. It seems that the differences in microstructure and hardness growth of the joint line are the main reasons for the strength increase in the UFSWed case compared to the FSWed sample.

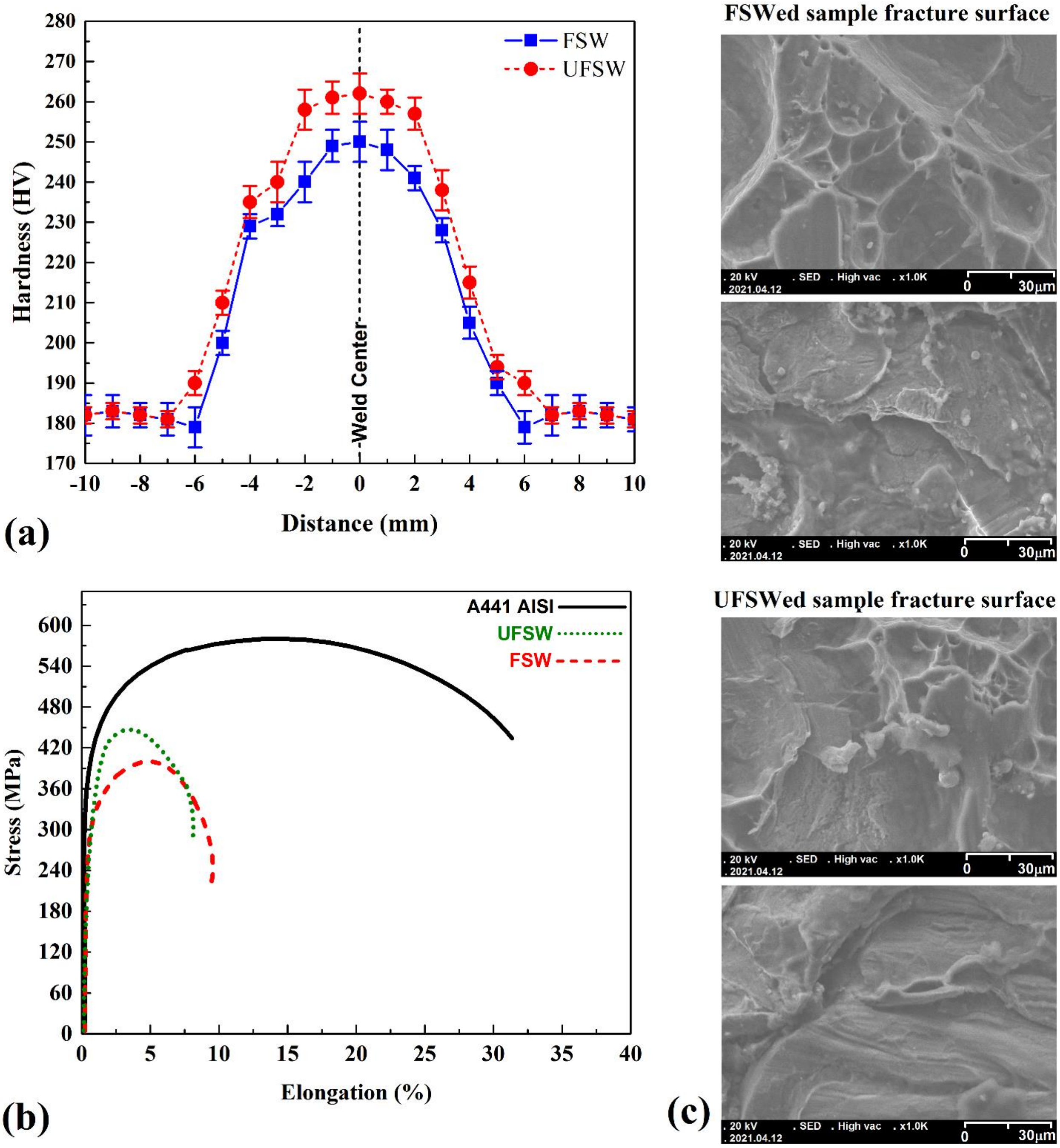

Figure 8. (**a**) Hardness of joint line at regular and underwater FSW cases. (**b**) Stress-strain graph of welded samples and (**c**) fracture surface of FSWed and UFSWed tensile samples.

5. Conclusions

In this research, CFD technique was used to simulate conventional and underwater FSW of low carbon steel plates. The results from simulation were validated by experimental test and the following consequences were achieved:

1. Due to recorded and simulated results, the heat production at the FSWed case (~1228 °C) was higher than the UFSWed (~1008 °C) joint. Owing to the smaller PHA at the leading edge of the tool and injecting the plasticized steel with higher viscosity into the SZ, the produced heat in the UFSW case decreased compared to the FSW sample. A close investigation showed that the main heat in UFSW case was produced by the tool shoulder.

2. The obtained results from the simulation revealed that the generated heat by tool shoulder in the UFSW (900 °C) case was higher than the FSW (786 °C) case, which means the high viscosity materials that were imported into the SZ decreased the heat generated by the tool pin.
3. The radiographic test from the FSWed and UFSWed joint lines did not show any defects. On the other hand, the results from the simulation of material velocity showed that the velocity of the plasticized steel in SZ of the FSWed (0.4 m/s) sample was 12% more than the UFSWed joint (~0.32 m/s). This conduct was caused in the lower flow ring angle of the material at the surface of the joint line in the underwater joint during the forward movement of the FSW tool.
4. The simulation results revealed higher strain-rate and lower viscosity of steel in the underwater joint compared to the SFWed case.
5. The investigation of welded samples microstructure showed that high cooling rate of the joint line in the underwater case decreased the grain size of the stir zone. The evaluation tensile strength of the welded samples specified a ~13.5 percent increase of ultimate tensile strength at the underwater joint compared to the regular FSW joint.

Author Contributions: Conceptualization, S.M., J.T., and H.A.D.; methodology, S.M. and H.A.D.; software, H.A.D.; validation, S.M., J.T., and H.A.D.; formal analysis, S.M., J.T., and H.A.D.; investigation, S.M. and H.A.D.; resources, S.M., J.T., and H.A.D.; data curation, H.A.D.; writing—original draft preparation, S.M., J.T., and H.A.D.; writing—review and editing, S.M., J.T., and H.A.D.; visualization, S.M. and H.A.D.; supervision, H.A.D.; project administration, H.A.D.; funding acquisition, S.M., J.T., and H.A.D. All authors have read and agreed to the published version of the manuscript.

Funding: This research received no external funding.

Institutional Review Board Statement: Not applicable.

Informed Consent Statement: Not applicable.

Data Availability Statement: Data sharing is not applicable to this article.

Conflicts of Interest: The authors declare no conflict of interest.

References

1. Khodabakhshi, F.; Derazkola, H.A.; Gerlich, A.P. Monte Carlo simulation of grain refinement during friction stir processing. *J. Mater. Sci.* **2020**, *55*, 13438–13456, doi:10.1007/s10853-020-04963-2.
2. Derazkola, H.A.; Khodabakhshi, F.; Simchi, A. Evaluation of a polymer-steel laminated sheet composite structure produced by friction stir additive manufacturing (FSAM) technology. *Polym. Test.* **2020**, *90*, 106690, doi:10.1016/j.polymertesting.2020.106690.
3. Aghajani Derazkola, H.; Kordani, N.; Aghajani Derazkola, H. Effects of friction stir welding tool tilt angle on properties of Al-Mg-Si alloy T-joint. *CIRP J. Manuf. Sci. Technol.* **2021**, *33*, 264–276, doi:10.1016/j.cirpj.2021.03.015.
4. Derazkola, H.A.; Khodabakhshi, F. A novel fed friction-stir (FFS) technology for nanocomposite joining. *Sci. Technol. Weld. Join.* **2020**, *25*, doi:10.1080/13621718.2019.1631534.
5. Janeczek, A.; Tomków, J.; Fydrych, D. The Influence of Tool Shape and Process Parameters on the Mechanical Properties of AW-3004 Aluminium Alloy Friction Stir Welded Joints. *Materials* **2021**, *14*, 3244.
6. Aghajani Derazkola, H.; Eyvazian, A.; Simchi, A. Submerged friction stir welding of dissimilar joints between an Al-Mg alloy and low carbon steel: Thermo-mechanical modeling, microstructural features, and mechanical properties. *J. Manuf. Process.* **2020**, *50*, 68–79, doi:10.1016/j.jmapro.2019.12.035.
7. Memon, S.; Paidar, M.; Mehrez, S.; Cooke, K.; Ojo, O.O.; Lankarani, H.M. Effects of materials positioning and tool rotational speed on metallurgical and mechanical properties of dissimilar modified friction stir clinching of AA5754-O and AA2024-T3 sheets. *Results Phys.* **2021**, *22*, 103962, doi:10.1016/j.rinp.2021.103962.
8. Mehta, K.P.; Patel, R.; Vyas, H.; Memon, S.; Vilaça, P. Repairing of exit-hole in dissimilar Al-Mg friction stir welding: Process and microstructural pattern. *Manuf. Lett.* **2020**, *23*, 67–70, doi:10.1016/j.mfglet.2020.01.002.
9. Memon, S.; Paidar, M.; Mehta, K.P.; Babaei, B.; Lankarani, H.M. Friction Spot Extrusion Welding on Dissimilar Materials AA2024-T3 to AA5754-O: Effect of Shoulder Plunge Depth. *J. Mater. Eng. Perform.* **2021**, *30*, 334–345, doi:10.1007/s11665-020-05387-4.
10. Paidar, M.; Memon, S.; Samusenkov, V.O.; Babaei, B.; Ojo, O.O. Friction spot extrusion welding-brazing of copper to aluminum alloy. *Mater. Lett.* **2021**, *285*, 129160, doi:10.1016/j.matlet.2020.129160.

11. Paidar, M.; Mehrez, S.; Babaei, B.; Memon, S.; Ojo, O.O.; Lankarani, H.M. Dissimilar welding of AA5083 to AZ31 Mg alloys using modified friction stir clinching brazing. *Mater. Lett.* **2021**, *301*, 129764, doi:10.1016/j.matlet.2021.129764.
12. Talebizadehsardari, P.; Musharavati, F.; Khan, A.; Sebaey, T.A.; Eyvaziana, A.; Derazkola, H.A. Underwater friction stir welding of Al-Mg alloy: Thermo-mechanical modeling and validation. *Mater. Today Commun.* **2021**, *26*, 101965, doi:10.1016/j.mtcomm.2020.101965.
13. Aghajani Derazkola, H.; Garcia, E.; Elyasi, M. Underwater friction stir welding of PC: Experimental study and thermo-mechanical modelling. *J. Manuf. Process.* **2021**, *65*, 161–173, doi:10.1016/j.jmapro.2021.03.034.
14. Bijanrostami, K.; Barenji, R.V.; Hashemipour, M. Effect of Traverse and Rotational Speeds on the Tensile Behavior of the Underwater Dissimilar Friction Stir Welded Aluminum Alloys. *J. Mater. Eng. Perform.* **2017**, *26*, 909–920, doi:10.1007/s11665-017-2506-0.
15. Baillie, P.; Campbell, S.W.; Galloway, A.M.; Cater, S.R.; McPherson, N.A. Friction stir welding of 6mm thick carbon steel underwater and in air. *Sci. Technol. Weld. Join.* **2015**, *20*, 585–593, doi:10.1179/1362171815Y.0000000042.
16. Derazkola, H.A.; Khodabakhshi, F. Underwater submerged dissimilar friction-stir welding of AA5083 aluminum alloy and A441 AISI steel. *Int. J. Adv. Manuf. Technol.* **2019**, *102*, 4383–4395, doi:10.1007/s00170-019-03544-1.
17. Liu, H.J.; Zhang, H.J.; Yu, L. Homogeneity of Mechanical Properties of Underwater Friction Stir Welded 2219-T6 Aluminum Alloy. *J. Mater. Eng. Perform.* **2011**, *20*, 1419–1422, doi:10.1007/s11665-010-9787-x.
18. Liu, H.J.; Zhang, H.J.; Yu, L. Effect of welding speed on microstructures and mechanical properties of underwater friction stir welded 2219 aluminum alloy. *Mater. Des.* **2011**, *32*, 1548–1553, doi:10.1016/j.matdes.2010.09.032.
19. Liu, H.; Zhang, H.; Huang, Y.; Yu, L. Mechanical properties of underwater friction stir welded 2219 aluminum alloy. *Trans. Nonferrous Met. Soc. China* **2010**, *20*, 1387–1391, doi:10.1016/S1003-6326(09)60309-5.
20. Sree Sabari, S.; Malarvizhi, S.; Balasubramanian, V.; Madusudhan Reddy, G. Experimental and numerical investigation on underwater friction stir welding of armour grade AA2519-T87 aluminium alloy. *Def. Technol.* **2016**, *12*, 324–333, doi:10.1016/j.dt.2016.02.003.
21. Tan, Y.B.; Wang, X.M.; Ma, M.; Zhang, J.X.; Liu, W.C.; Fu, R.D.; Xiang, S. A study on microstructure and mechanical properties of AA 3003 aluminum alloy joints by underwater friction stir welding. *Mater. Charact.* **2017**, *127*, 41–52, doi:10.1016/j.matchar.2017.01.039.
22. Kishta, E.E.; Darras, B. Experimental investigation of underwater friction-stir welding of 5083 marine-grade aluminum alloy. *Proc. Inst. Mech. Eng. Part B J. Eng. Manuf.* **2014**, *230*, 458–465, doi:10.1177/0954405414555560.
23. Hajinezhad, M.; Azizi, A. Numerical analysis of effect of coolant on the transient temperature in underwater friction stir welding of Al6061-T6. *Int. J. Adv. Manuf. Technol.* **2016**, *83*, 1241–1252, doi:10.1007/s00170-015-7652-7.
24. Zhao, Y.; Wang, Q.; Chen, H.; Yan, K. Microstructure and mechanical properties of spray formed 7055 aluminum alloy by underwater friction stir welding. *Mater. Des.* **2014**, *56*, 725–730, doi:10.1016/j.matdes.2013.11.071.
25. Mahto, R.P.; Gupta, C.; Kinjawadekar, M.; Meena, A.; Pal, S.K. Weldability of AA6061-T6 and AISI 304 by underwater friction stir welding. *J. Manuf. Process.* **2019**, *38*, 370–386, doi:10.1016/j.jmapro.2019.01.028.
26. Mohan, D. G.; Tomków, J.; Gopi, S. Induction assisted hybrid friction stir welding of dissimilar materials AA5052 aluminium alloy and X12Cr13 stainless steel. *Adv. Mater. Sci.* **2021**, *21*, 17–30.
27. Eyvazian, A.; Hamouda, A.; Tarlochan, F.; Derazkola, H.A.; Khodabakhshi, F. Simulation and experimental study of underwater dissimilar friction-stir welding between aluminium and steel. *J. Mater. Res. Technol.* **2020**, *9*, 3767–3781, doi:10.1016/j.jmrt.2020.02.003.
28. Zhang, J.; Shen, Y.; Yao, X.; Xu, H.; Li, B. Investigation on dissimilar underwater friction stir lap welding of 6061-T6 aluminum alloy to pure copper. *Mater. Des.* **2014**, *64*, 74–80, doi:10.1016/j.matdes.2014.07.036.
29. Zhao, Y.; Jiang, S.; Yang, S.; Lu, Z.; Yan, K. Influence of cooling conditions on joint properties and microstructures of aluminum and magnesium dissimilar alloys by friction stir welding. *Int. J. Adv. Manuf. Technol.* **2016**, *83*, 673–679, doi:10.1007/s00170-015-7624-y.
30. Zhao, Y.; Lu, Z.; Yan, K.; Huang, L. Microstructural characterizations and mechanical properties in underwater friction stir welding of aluminum and magnesium dissimilar alloys. *Mater. Des.* **2015**, *65*, 675–681, doi:10.1016/j.matdes.2014.09.046.
31. Miyamori, T.; Sato, Y.; Kokawa, H. *Influence of Underwater Operation on Friction Stir Welding of Medium Carbon Steel BT—Friction Stir Welding and Processing IX*; Hovanski, Y., Mishra, R., Sato, Y., Upadhyay, P., Yan, D., Eds.; Springer International Publishing: Cham, Switzerland, 2017; pp. 23–28.
32. Wang, Z.W.; Ma, G.N.; Yu, B.H.; Xue, P.; Xie, G.M.; Zhang, H.; Ni, D.R.; Xiao, B.L.; Ma, Z.Y. Improving mechanical properties of friction-stir-spot-welded advanced ultra-high-strength steel with additional water cooling. *Sci. Technol. Weld. Join.* **2020**, *25*, 336–344, doi:10.1080/13621718.2019.1706259.
33. Salimi, S.; Bahemmat, P.; Haghpanahi, M. Study on residual stresses caused by underwater friction stir welding: FE modeling and ultrasonic measurement. *Proc. Inst. Mech. Eng. Part E J. Process Mech. Eng.* **2018**, *233*, 118–137, doi:10.1177/0954408917751963.
34. Mirzaei, M.; Asadi, P.; Fazli, A. Effect of Tool Pin Profile on Material Flow in Double Shoulder Friction Stir Welding of AZ91 Magnesium Alloy. *Int. J. Mech. Sci.* **2020**, *183*, 105775, doi:10.1016/j.ijmecsci.2020.105775.
35. Iqbal, M.P.; Tripathi, A.; Jain, R.; Mahto, R.P.; Pal, S.K.; Mandal, P. Numerical modelling of microstructure in friction stir welding of aluminium alloys. *Int. J. Mech. Sci.* **2020**, *185*, 105882, doi:10.1016/j.ijmecsci.2020.105882.
36. Zhao, W.; Wu, C.; Shi, L. Acoustic induced antifriction and its effect on thermo-mechanical behavior in ultrasonic assisted friction stir welding. *Int. J. Mech. Sci.* **2021**, *190*, 106039, doi:10.1016/j.ijmecsci.2020.106039.
37. Aghajani Derazkola, H.; Khodabakhshi, F. Intermetallic compounds (IMCs) formation during dissimilar friction-stir welding of AA5005 aluminum alloy to St-52 steel: Numerical modeling and experimental study. *Int. J. Adv. Manuf. Technol.* **2019**, *100*, 2401–2422, doi:10.1007/s00170-018-2879-8.

38. Eyvazian, A.; Hamouda, A.M.; Aghajani Derazkola, H.; Elyasi, M. Study on the effects of tool tile angle, offset and plunge depth on friction stir welding of poly(methyl methacrylate) T-joint. *Proc. Inst. Mech. Eng. Part B J. Eng. Manuf.* **2019**, *234*, 773–787, doi:10.1177/0954405419889180.
39. Muhammad, N.A.; Wu, C. Evaluation of capabilities of ultrasonic vibration on the surface, electrical and mechanical behaviours of aluminium to copper dissimilar friction stir welds. *Int. J. Mech. Sci.* **2020**, *183*, 105784, doi:10.1016/j.ijmecsci.2020.105784.
40. Hernández, C.A.; Ferrer, V.H.; Mancilla, J.E.; Martínez, L.C. Three-dimensional numerical modeling of the friction stir welding of dissimilar steels. *Int. J. Adv. Manuf. Technol.* **2017**, *93*, 1567–1581, doi:10.1007/s00170-017-0578-5.
41. Yang, C.; Hou, X. Iterative two-layer thermal design strategy for step sandwich antenna of space solar power satellite using modified constrained multi-objective optimization. *Aerosp. Sci. Technol.* **2021**, *118*, 106987, doi:10.1016/j.ast.2021.106987.
42. Yang, C.; Hou, X.; Chang, S. A synchronous placement and size-based multi-objective optimization method for heat dissipation design on antenna module of space solar power satellite. *Sustain. Energy Technol. Assess.* **2021**, *45*, 101183, doi:10.1016/j.seta.2021.101183.
43. Lambiase, F.; Derazkola, H.A.; Simchi, A. Friction Stir Welding and Friction Spot Stir Welding Processes of Polymers—State of the Art. *Materials* **2020**, *13*, 2291.
44. Aghajani Derazkola, H.; Simchi, A. Experimental and thermomechanical analysis of friction stir welding of poly(methyl methacrylate) sheets. *Sci. Technol. Weld. Join.* **2017**, *23*, 209–218, doi:10.1080/13621718.2017.1364896.
45. Aghajani Derazkola, H.; Simchi, A. Experimental and thermomechanical analysis of the effect of tool pin profile on the friction stir welding of poly(methyl methacrylate) sheets. *J. Manuf. Process.* **2018**, *34*, 412–423, doi:10.1016/j.jmapro.2018.06.015.
46. Derazkola, H.A.; Khodabakhshi, F.; Simchi, A. Friction-stir lap-joining of aluminium-magnesium/poly-methyl-methacrylate hybrid structures: Thermo-mechanical modelling and experimental feasibility study. *Sci. Technol. Weld. Join.* **2018**, *23*, 35–49, doi:10.1080/13621718.2017.1323441.
47. Robe, H.; Claudin, C.; Bergheau, J.-M.; Feulvarch, E. R-ALE simulation of heat transfer during friction stir welding of an AA2xxx/AA7xxx joint on a large process window. *Int. J. Mech. Sci.* **2019**, *155*, 31–40, doi:10.1016/j.ijmecsci.2019.02.029.
48. Buffa, G.; Fratini, L.; Impero, F.; Masnata, A.; Scherillo, F.; Squillace, A. Surface and mechanical characterization of stationary shoulder friction stir welded lap joints: Experimental and numerical approach. *Int. J. Mater. Form.* **2020**, *13*, 725–736, doi:10.1007/s12289-020-01574-9.
49. Rana, P.K.; Narayanan, R.G. Numerical and experimental response of FSSW of AA5052-H32/epoxy/AA5052-H32 sandwich sheets with varying core properties. *Int. J. Mater. Form.* **2020**, 1–21, doi:10.1007/s12289-020-01596-3.
50. Buffa, G.; Fratini, L.; Micari, F.; Shivpuri, R. Material Flow in FSW of T-joints: Experimental and Numerical Analysis. *Int. J. Mater. Form.* **2008**, *1*, 1283–1286, doi:10.1007/s12289-008-0137-6.
51. Yu, P.; Wu, C.; Shi, L. Analysis and characterization of dynamic recrystallization and grain structure evolution in friction stir welding of aluminum plates. *Acta Mater.* **2021**, *207*, 116692, doi:10.1016/j.actamat.2021.116692.
52. Wang, X.; Gao, Y.; Liu, X.; McDonnell, M.; Feng, Z. Tool-workpiece stick-slip conditions and their effects on torque and heat generation rate in the friction stir welding. *Acta Mater.* **2021**, *213*, 116969, doi:10.1016/j.actamat.2021.116969.
53. Yang, H.; Zhao, H.; Xu, X.; Zhou, L.; Zhao, H.; Liu, H. Effect of Stirring Pin Rotation Speed on Microstructure and Mechanical Properties of 2A14-T4 Alloy T-Joints Produced by Stationary Shoulder Friction Stir Welding. *Materials* **2021**, *14*, 1938.
54. Gale, W.F.; Totemeier, T.C.B.T.-S.M.R.B. (Eds.) *14—General Physical Properties*, 8th ed.; Butterworth-Heinemann: Oxford, UK, 2004; pp. 14–45, ISBN 978-0-7506-7509-3.
55. Gale, W.F.; Totemeier, T.C.B.T.-S.M.R.B. (Eds.) *13—Diffusion in Metals*, 8th ed.; Butterworth-Heinemann: Oxford, UK, 2004; pp. 13–120, ISBN 978-0-7506-7509-3.
56. Gale, W.F.; Totemeier, T.C.B.T.-S.M.R.B. (Eds.) *3—General Physical and Chemical Constants*, 8th ed.; Butterworth-Heinemann: Oxford, UK, 2004; pp. 3–11, ISBN 978-0-7506-7509-3.
57. Gale, W.F.; Totemeier, T.C.B.T.-S.M.R.B. (Eds.) *12—Gas–Metal Systems*, 8th ed.; Butterworth-Heinemann: Oxford, UK, 2004; pp. 12–28, ISBN 978-0-7506-7509-3.
58. Huang, Y.; Xie, Y.; Meng, X.; Lv, Z.; Cao, J. Numerical design of high depth-to-width ratio friction stir welding. *J. Mater. Process. Technol.* **2018**, *252*, 233–241, doi:10.1016/j.jmatprotec.2017.09.029.
59. Yang, C. An adaptive sensor placement algorithm for structural health monitoring based on multi-objective iterative optimization using weight factor updating. *Mech. Syst. Signal Process.* **2021**, *151*, 107363, doi:10.1016/j.ymssp.2020.107363.
60. CAO, Z.; SUN, Y.; ZHOU, C.; WAN, Z.; YANG, W.; REN, L.; HU, L. Cellular automaton simulation of dynamic recrystallization behavior in V-10Cr-5Ti alloy under hot deformation conditions. *Trans. Nonferrous Met. Soc. China* **2019**, *29*, 98–111, doi:10.1016/S1003-6326(18)64919-2.
61. Huang, G.Q.; Yan, Y.F.; Wu, J.; Shen, Y.F.; Gerlich, A.P. Microstructure and mechanical properties of fine-grained aluminum matrix composite reinforced with nitinol shape memory alloy particulates produced by underwater friction stir processing. *J. Alloys Compd.* **2019**, *786*, 257–271, doi:10.1016/j.jallcom.2019.01.364.
62. Yang, X.; Yan, Z.; Dong, P.; Cheng, B.; Zhang, J.; Zhang, T.; Zhang, H.; Wang, W. Surface modification of aluminum alloy by incorporation of AlCoCrFeNi high entropy alloy particles via underwater friction stir processing. *Surf. Coatings Technol.* **2020**, *385*, 125438, doi:10.1016/j.surfcoat.2020.125438.
63. Heirani, F.; Abbasi, A.; Ardestani, M. Effects of processing parameters on microstructure and mechanical behaviors of underwater friction stir welding of Al5083 alloy. *J. Manuf. Process.* **2017**, *25*, 77–84, doi:10.1016/j.jmapro.2016.11.002.

64. Wahid, M.A.; Khan, Z.A.; Siddiquee, A.N. Review on underwater friction stir welding: A variant of friction stir welding with great potential of improving joint properties. *Trans. Nonferrous Met. Soc. China* **2018**, *28*, 193–219, doi:10.1016/S1003-6326(18)64653-9.
65. Singh, V.P.; Patel, S.K.; Kuriachen, B. Mechanical and microstructural properties evolutions of various alloys welded through cooling assisted friction-stir welding: A review. *Intermetallics* **2021**, *133*, 107122, doi:10.1016/j.intermet.2021.107122.
66. Rathinasuriyan, C.; Pavithra, E.; Sankar, R.; Kumar, V.S.S. Current Status and Development of Submerged Friction Stir Welding: A Review. *Int. J. Precis. Eng. Manuf. Technol.* **2021**, *8*, 687–701, doi:10.1007/s40684-020-00187-6.
67. Liang, H.; Yan, K.; Wang, Q.; Zhao, Y.; Liu, C.; Zhang, H. Improvement in Joint Strength of Spray-Deposited Al-Zn-Mg-Cu Alloy in Underwater Friction Stir Welding by Altered Temperature of Cooling Water. *J. Mater. Eng. Perform.* **2016**, *25*, 5486–5493, doi:10.1007/s11665-016-2383-y.
68. MOAREF, A.; RABIEZADEH, A. Microstructural evaluation and tribological properties of underwater friction stir processed CP-copper and its alloy. *Trans. Nonferrous Met. Soc. China* **2020**, *30*, 972–981, doi:10.1016/S1003-6326(20)65269-4.
69. Tiwari, A.; Pankaj, P.; Suman, S.; Biswas, P. CFD Modelling of Temperature Distribution and Material Flow Investigation During FSW of DH36 Shipbuilding Grade Steel. *Trans. Indian Inst. Met.* **2020**, *73*, 2291–2307, doi:10.1007/s12666-020-02030-7.
70. Hasan, A.F.; Bennett, C.J.; Shipway, P.H. A numerical comparison of the flow behaviour in Friction Stir Welding (FSW) using unworn and worn tool geometries. *Mater. Des.* **2015**, *87*, 1037–1046, doi:10.1016/j.matdes.2015.08.016.
71. Colegrove, P.A.; Shercliff, H.R.; Zettler, R. Model for predicting heat generation and temperature in friction stir welding from the material properties. *Sci. Technol. Weld. Join.* **2007**, *12*, 284–297, doi:10.1179/174329307X197539.
72. Sun, Z.; Wu, C.S. Influence of tool thread pitch on material flow and thermal process in friction stir welding. *J. Mater. Process. Technol.* **2020**, *275*, 116281, doi:10.1016/j.jmatprotec.2019.116281.
73. Dong, J.; Zhang, D.; Luo, X.; Zhang, W.; Zhang, W.; Qiu, C. EBSD study of underwater friction stir welded AA7003-T4 and AA6060-T4 dissimilar joint. *J. Mater. Res. Technol.* **2020**, *9*, 4309–4318, doi:10.1016/j.jmrt.2020.02.056.
74. Yang, X.; Zhai, X.; Dong, P.; Yan, Z.; Cheng, B.; Zhang, H.; Wang, W. Interface characteristics of high-entropy alloy/Al-Mg composites by underwater friction stir processing. *Mater. Lett.* **2020**, *275*, 128200, doi:10.1016/j.matlet.2020.128200.